Rigid-elastic Coupling Dynamic Model and Dynamic Characteristics of a Spring-type of Traction Robot

Jianguo Zhao[1,2,3,*] – Binfan Wang[1,3] – Qingyou Liu[1,3] – Guorong Wang[1,3] – Xiangfeng Zeng[4]

[1]Southwest Petroleum University, School of Mechantronic Engineering, China
[2]Sichuan Provincial Key Lab of Process Equipment and Control, China
[3]Southwest Petroleum University, Energy Equipment Institute, China
[4]Yunnan Shuifu Yuntianhua Co., China

The traditional anchoring mechanism of the traction robot is rigid and is easily stuck in the wellbore. To solve this problem, a novel anchoring mechanism is proposed based on the spring-type of anchoring mechanism of the inclined block. The key to the movement of the traction robot is whether the traction robot can be anchored in the wellbore under the action of the traction force. Therefore, a rigid-elastic coupling dynamic model of the spring-type of anchoring mechanism under the action of the traction force was established. On this basis, the effects of span, width, thickness, and chamfer parameters on the anchoring performance of the spring-type of traction robot were analysed to design the optimal structure of the anchoring arm. Through the experimental comparison, it was determined that the error between the theoretical supporting force and the experimental supporting force was only 6.1 %, and the error of the simulated maximum traction force and experimental maximum traction force was 4.9 %. The traction robot can provide a maximum traction force of 14262 N in 178 mm (7-inch) of wellbore pipe. Thus, experiments verified the correctness of the rigid-elastic coupling dynamic model. The research results of this paper lay a foundation for the structural design and engineering application of a spring-type of traction robot. It can effectively ensure the downhole safety of oil and gas wells.
Keywords: spring-type of traction robot, spring-type of rigid-elastic coupling dynamic model, spring-type of anchoring mechanism, motion anchoring

Highlights
- *A novel spring-type of anchoring mechanism of traction robot based on inclined blocks is proposed, which provides a large traction force for the robot and can avoid being stuck.*
- *The rigid-elastic coupling dynamic model of the spring-type of anchoring mechanism is established.*
- *The calculation method of boundary conditions of self-anchoring of the traction robot (safe or not) is created.*
- *The maximum traction forces under different structural parameters have been obtained, and the correctness of the theoretical maximum traction force has been verified by experiments.*

0 INTRODUCTION

Horizontal well exploitation has become an important way to increase the recovery of oil and gas fields. It is mainly applied to the exploration and development of deep-sea and complex petroleum resources. It is increasingly difficult to deliver drilling tools as the depth of horizontal wells and the length of horizontal sections continue to increase. Compared with several methods, such as coiled tubing conveyance [1] and [2], drill pipe conveyance, and pump-in conveyance, the conveying method of downhole traction robots [3] to [5] can deliver instruments quickly and accurately, as well as significantly save time and reduce costs [6].

According to the movement mode, downhole traction robots can be divided into wheeled-type [7] to [10], telescopic-type [11] and [12], crawler-type [13] and [14], etc. Among them, wheeled and telescopic types are the most widely used in engineering. The conventional wheel-type traction robot has a group of expandable and collapsible anchoring arms, which

hold the driving wheels against the wellbore wall. The rotating driving wheels drive the wheel-type traction robot to move in the horizontal well by the friction force between the driving wheel and the wellbore. The conventional telescopic traction robot is anchored in the wellbore wall by two or more sets of anchoring arms that can be opened and closed alternately. One group of anchoring arms is held stationary on the wellbore wall. At this point, another set of cylinders or motors slides towards or behind each other to achieve directional movement of the robot in the wellbore. For telescopic traction robot, rigid anchoring arms are mostly adopted between the anchoring mechanism and the wellbore wall to anchor the wellbore wall to perform traction action. The rigid anchoring arm has more constraints, which leads to fewer degrees of freedom in the mechanism, so it easily becomes stuck during the working process.

In addition, the anchoring mechanism of telescopic traction robot can adopt an elastic anchoring method. However, most of the elastic

anchoring mechanisms designed by Gao et al. [15] and Liu et al. [16] and [17] are connected with rods and pins, at which points the forces on them are mainly concentrated. The position of the connecting rod and pin cannot achieve the strength requirements, so that the mechanism is deformed. Moreover, the schemes of the elastic anchoring methods only considered the motion characteristics under the rigid conditions but did not optimize its anchoring structures or determine its maximum traction force.

Therefore, based on previous studies, a novel telescopic downhole traction robot based on the spring-type of anchoring mechanism of the inclined block [18] is proposed in this paper. The traction robot has the characteristics of large traction force and automatic un-anchoring, which can to some extent prevent the occurrence of being stuck. This paper focuses on analysing the influencing factors of the spring-type of anchoring mechanism and optimizing its structures. The maximum traction force of the spring-type of anchoring mechanism under different wellbores is determined.

1 WORKING MECHANISM

On the basis of analysing and determining the strengths and weaknesses of existing traction robots, this paper proposes a spring-type of hydraulic telescopic downhole traction robot. It adopts a leaf spring with elastic restoring force as the anchoring arm, which can provide greater traction force while better adapting to the wellbore wall. This traction robot is lowered into the horizontal section through coiled tubing. The primary function of the robot is to deliver downhole pipe strings in horizontal wells or large displacement

wells for other operations, such as logging and well workovers. The traction robot connects coiled tubing at the end and the downhole tools at the front, and its power and signals are transmitted through the cables and signal lines inside the coiled tubing. The application form of the robot is shown in Fig. 1.

It can be seen from Fig. 1 that the spring-type of telescopic downhole traction robot includes a front working section, a rear working section, and a control section. The front working section includes a front anchoring mechanism and a front telescopic mechanism, and the rear working section includes a rear anchoring mechanism and a rear telescopic mechanism. The executive parts of the working mechanism include four double-acting hydraulic cylinders (front support cylinder, front telescopic cylinder, rear support cylinder, rear telescopic cylinder). The action mechanism will be described below in conjunction with the action sequence in Fig. 2.

(1) From the initial status to status A: The hydraulic oil is injected into the front support cylinder, and the push rod of the front support cylinder is pushed to move to the right. The anchoring arms extend to anchor the wellbore wall.

(2) From status A to status B: The front and rear telescopic cylinders are simultaneously injected with hydraulic oil. The control section and rear working section simultaneously walk forward a telescopic cylinder stroke S. At this point, the traction robot has completed the first forward motion.

(3) From status B to status C: The rear support cylinder is injected with hydraulic oil and pushes the rear support cylinder push rod to move to the
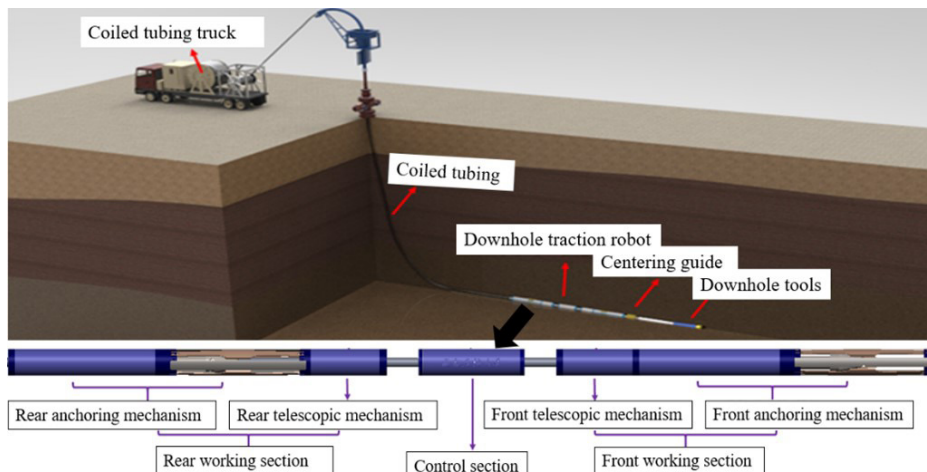

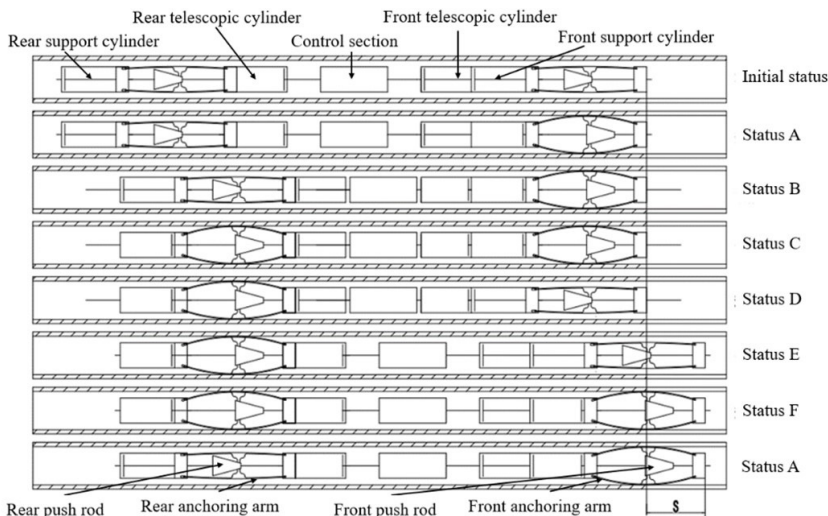**Fig. 1.** *Application form of spring-type of hydraulic telescopic downhole traction robot*

Fig. 2. *Schematic diagram of the working mechanism of the downhole traction robot*

right. Under the action of the rear push rod joint, the rear anchoring arms extend to anchor the wellbore wall to prepare for the alternate work of the front and rear working sections.

(4) From status C to status D: The front support cylinder is injected with hydraulic oil. At this time, the front anchor arms are restored to their initial state to prepare for the movement of the rear telescopic cylinder.

(5) From status D to status E: Hydraulic oil is injected simultaneously into the rear telescopic cylinder and the front telescopic cylinder. The control section and the front working section are simultaneously crawling forward for one telescopic cylinder stroke *S*. At this time, the traction robot completes the first stretch.

As shown in Fig. 2, it is a complete motion cycle of the traction robot from the initial status to status *F*. The front and rear working section are operated alternately to achieve forward telescopic crawling.

2 DYNAMIC CHARACTERISTICS

The mechanical model of the spring-type of anchoring mechanism is shown in Fig. 3 during the traction process. In this chapter, the relationship between the supporting force F_S of the supporting cylinder, the traction force F_T and the elastic restoring force F_2 can be obtained through the analysis of the mechanical model. The elastic restoring force and the maximum stress of the spring-type of anchoring arm with different structural sizes can be obtained using ABAQUS simulation analysis [19]. The
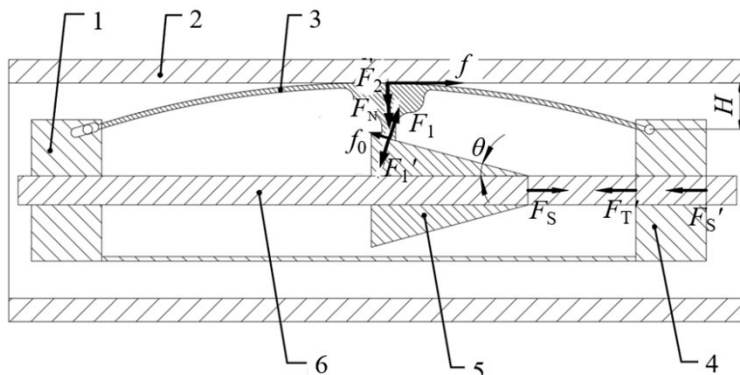

Fig. 3. *Schematic diagram of stress analysis of spring-type of anchoring mechanism; 1 left support frame, 2 wellbore pipe, 3 spring-type of anchoring arm, 4 right support frame, 5 push rod joint, and 6 central axis*

optimal structure of the spring-type of anchoring arm that meets the safe mechanical conditions and can overcome the friction force of the hydraulic cylinder seal ring to achieve automatic recovery will be determined under no-load conditions. Finally, the values of F_S and F_2 of the spring-type of anchoring arm with the optimal structural size in different sizes of the wellbore are obtained.

2.1 Mechanical Characteristics of Traction Process of Spring-Type of Anchoring Mechanism

After the spring-type of anchoring mechanism of the traction robot anchors the wellbore wall, the telescopic mechanism of the traction robot starts to drag the downhole tool to move forward. At this point, the friction between three spring-types of anchoring arms and the wellbore wall will overcome the load traction force of the downhole tools to achieve forward motion.

It can be seen from Fig. 3 that the push rod joint is subjected to the supporting force F_S and the reaction force of supporting force F_1' in the process of rightward movement. A spring-type of anchoring arm is subjected to the supporting force F_1, the wellbore wall supporting force F_N, its elastic restoring force F_2, and the whole anchoring mechanism is subjected to the friction force f. At the same time, the left support frame of the spring-type of anchoring arm is solidly connected to the right support frame. In the process of moving the push rod joint to the right, the right support frame will generate the reaction force F_S', which is equal to the supporting force F_S and opposite to the direction, and the load reaction force F_T' which makes the downhole tools achieve forward motion.

Take a single spring-type of anchoring arm as the research object. F_1 is the supporting force generated by the push rod joint. F_N is the supporting force generated by the wellbore wall. F_S' is the reaction force of the supporting force. F_T' is the reaction force of the traction force. f is the friction force generated by the wellbore wall to the whole anchoring mechanism. Three spring-types of anchoring arms are uniformly distributed along the central axis in space, so that the resultant force of three frictional forces between three spring-types of anchoring arms and push rod joint is 0 N in the radial direction. The gap between three spring-types of anchoring arms and push rod joint is matched, and there is a lubrication device, so the friction between them can be ignored. Through ABAQUS simulated analysis, θ is selected as 13.6° according to the design structure. H is the radial displacement of the spring-type of anchoring arm, which is determined

by the different inner diameters of the wellbore. According to the mechanical equilibrium relationship, there is the following relationship equation.

According to $\Sigma X=0$, the following equation can be obtained:

$$F_1 \sin\theta + \frac{f}{3} = \frac{F_s'}{3} + \frac{F_T'}{3}. \tag{1}$$

According to $\Sigma Y=0$, the following equation can be obtained:

$$F_1 \cos\theta = F_2 + F_N. \tag{2}$$

In addition, it is assumed that the friction coefficient between the wellbore wall and spring-type of anchoring arm is μ, which is taken a value as 0.25 (the value of μ is 0.2 to 0.3, and the intermediate value of 0.25 is taken for theoretical research). Then there is the relationship equation:

$$\frac{f}{3} = \mu F_N. \tag{3}$$

Substituting Eqs. (2) and (3) into Eq. (1) yields:

$$\left(\frac{f}{3\mu} + F_2\right)\tan\theta + \frac{f}{3} = \frac{F_s'}{3} + \frac{F_T'}{3}. \tag{4}$$

For the traction robot to crawl forward, the friction force f must be greater than or equal to the traction force F_T' on the traction robot, namely:

$$f \geq F_T'. \tag{5}$$

If the friction force is equal to the traction force of the traction robot, the relationship between the supporting force F_S of the support cylinder and the reaction force F_T' of the traction force can be derived by bringing Eq. (5) into Eq. (4):

$$F_s' = \frac{F_T'}{\mu}\tan\theta + 3F_2\tan\theta. \tag{6}$$

In Eq. (6), the reaction force F_T' of traction force is determined by the load. From Eq. (6), the supporting force F_S can be obtained to overcome different load traction forces in wellbores with different inner diameters.

2.2 Optimization Research of Structure Parameters of Spring-type of Traction Robot

The spring-type of anchoring arm of the traction robot is designed with the purpose of the leaf spring. When the traction robot has unexpected conditions in the well (such as power failure, solenoid valve out of control), the leaf spring can use its elastic restoring

force to overcome the friction generated by the seal in the support cylinder to avoid being stuck. The traction robot has two support cylinders, and the O-ring is a seal inside the support cylinder. Therefore, it is necessary to calculate the size of the friction resistance generated by the O-ring [20] in the support cylinder. Xu [21], Xiao [22], and Zuo and Zhang [23] studied the friction force generated by the O-ring in the hydraulic cylinder. From the design dimensions and relevant parameters of the traction robot, the frictional resistance of the sealing ring that needs to be overcome is 647 N when the piston is automatically reset by the restoring force of the leaf spring. Therefore, the leaf spring must fulfil this restoring force to achieve the function of automatic un-anchoring of the spring-type of anchoring mechanism.

From Eq. (6), it can be known that the main factor affecting the supporting force under the same wellbore and the traction force is the elastic restoring force of the spring-type of anchoring arm. Therefore, ABAQUS is used to simulate the span, thickness, width, and chamfer that affect the elastic restoring force of the spring leaf. The spring-type of anchoring arms are deformed under force, and its different radial displacements generate the corresponding elastic restoring forces. The design diameter of the traction robot is 118 mm, and it is suitable for a maximum pipe diameter of 178 mm (inner diameter (ID) 166 mm) wellbore. Therefore, for a 178 mm wellbore, the radial displacement H of the spring-type of anchoring arm is 24 mm, as shown in Fig. 3. Consequently, it is necessary to obtain the elastic restoring force with radial displacement of 24 mm.

According to the outside diameter of the traction robot and the design installation requirements, each parameter of the spring-type of anchoring arm is shown in Fig. 4, and the values are taken as illustrated in Table 1.
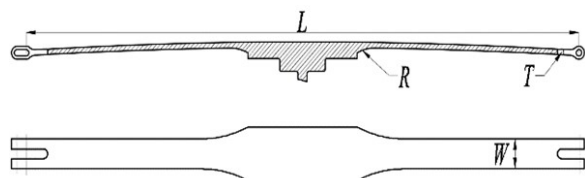
Fig. 4. *Schematic diagram of the spring-type of anchoring arm*

Under the same width, thickness, and chamfering radius of the spring, the changes of the elastic restoring force and the maximum stress of the spring with different spans are shown in Fig. 5.

Table 1. *The value of each parameter of anchoring arm*

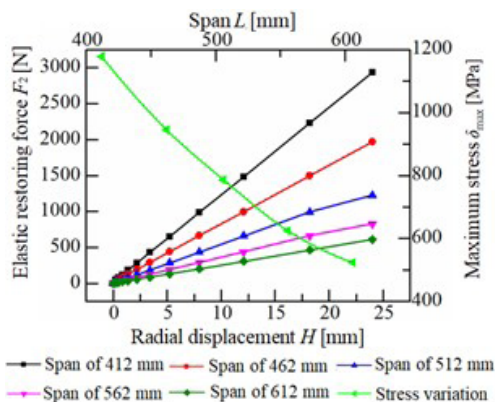| Designation	Value [mm]				
Span (L)	412	462	512	562	612
Width (W)	25	30	35	40	45
Thickness (T)	4	4.5	5	5.5	6
Chamfering radius (R)	20	40	60	80	100

Fig. 5. *Change of elastic force and stress with span*

It can be seen from Fig. 5 that the larger the span of the leaf spring had, the smaller the maximum stress and the elastic restoring force would become. When the radial displacement of the leaf spring was 24 mm, the elastic restoring force of the leaf spring with a span of 412 mm was the largest (2,907 N). However, its maximum stress had exceeded the yield limit of the material (the material of 60Si2Mn, the yield strength of 1,176 MPa), resulting in plastic deformation. The leaf spring with a span of 612 mm had the smallest elastic restoring force (611 N), but the leaf spring could not overcome the frictional resistance of the O-ring. Therefore, the elastic restoring force of 462 mm, which was larger and much lower than the yield strength of the material, was the optimal value of the leaf spring span.

In the case of a spring span of 462 mm with the same width and thickness, the changes in the elastic restoring force and the maximum stress of the spring with different chamfer radii are shown in Fig. 6.

It can be seen from Fig. 6 that the maximum stress was larger and should not be selected when the chamfering radius is 20 mm and 100 mm. The elastic restoring forces of the spring of the rest of the chamfer radii were similar, but the chamfer radius of 40 mm was the smallest maximum stress. Considering the yield limit and the elastic restoring force, the chamfering radius of 40mm was the optimal value of the chamfering radius of the leaf spring.
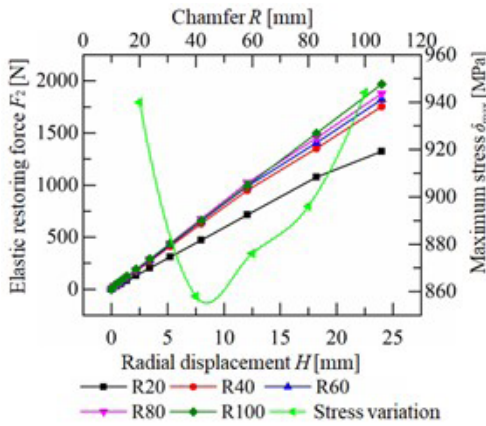
Fig. 6. *Change of elastic force and stress with chamfer*

In the case of a spring span of 462 mm, chamfer radius of 40 mm, and the same width, the changes in the elastic restoring force and the maximum stress of the spring with different thicknesses are shown in Fig. 7.

Similarly, the elastic restoring force and the maximum stress were positively correlated with the thickness by the analysis in Fig. 7. If the leaf spring was too thin, its stress met the material requirements, but its elastic restoring force did not satisfy the requirements. If the leaf spring was too thick, its elastic restoring force met the requirements, but its stress was extremely close to the yield limit of the material and did not meet the material requirements. Under the condition that other parameters remained unchanged if the thickness of the spring was selected as 5 mm, the maximum elastic restoring force was 1,753 N, and the maximum stress was 858 MPa. Both the restoring force and stress were suitable, so the thickness of 5mm was the optimal value in the spring leaf.
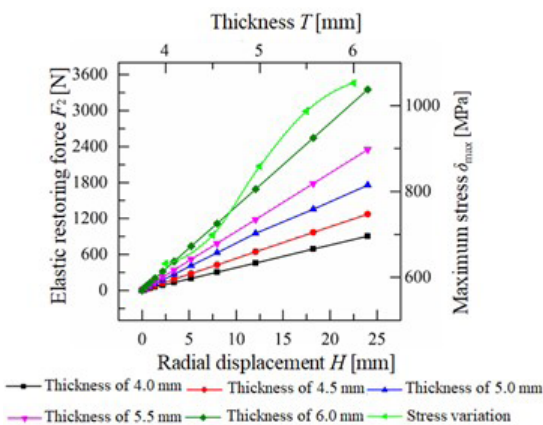

Fig. 7. *Change of elastic force and stress with thickness*

The variation curves of elastic restoring force and maximum stress for different widths of the leaf spring at a span of 462 mm, a chamfer radius of 40 mm, and a thickness of 5 mm are shown in Fig. 8.
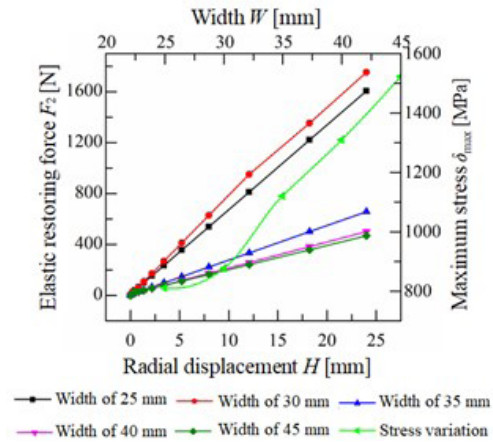

Fig. 8. *Change of elastic force and stress with width*

According to the analysis in Fig. 8, with the increase of the width of the spring, the elastic restoring force of the spring increased first and then decreased, and the maximum stress of the spring increased gradually. When the width of the leaf spring was 30 mm, the maximum elastic restoring force of the leaf spring was 1,753 N, and the maximum stress was 853 MPa. When the spring width was 45 mm, the maximum elastic restoring force of the spring was at least 451 N, and the maximum stress was 1,523 MPa. Obviously, the reason for the first increase in the elastic restoring force of the leaf spring was that its maximum stress was within the yield limit of the material. In addition, the reason for the sudden sharp decrease was that its maximum stress had exceeded the yield limit of the material, resulting in the plastic deformation. At a width of 35 mm, the analysis of the maximum stress diagram illustrated that the leaf spring had undergone plastic deformation in the weaker place, where is the chamfer of the spring of anchoring arm. Therefore, when the width of the spring piece was 30 mm, the stress was smaller and the elastic restoring force was appropriate. The width of 30 mm was the optimal value of the leaf spring width.

After the optimization of the structure parameters of the leaf spring, the final structure of the spring-type of anchoring arm was chosen to have a span of 462 mm, a chamfer radius of 40 mm, a width of 30 mm and a thickness of 5 mm. Through the data analysis of ABAQUS simulation, the relationship between the

restoring force F_2 and the radial displacement H of the spring arm can be obtained. The relationship is shown in Eq. (7):

$$F_2 = 14.7 + 73.7H. \qquad (7)$$

Bring Eq. (7) into Eq. (6) to obtain the final expression of the supporting force required by the traction robot:

$$F_s = 3 \times (14.7 + 7H) \tan\theta + \frac{F_T'}{\mu} \tan\theta. \qquad (8)$$

Taking the radial displacement H (0 mm to 24 mm) as the independent variable and the supporting cylinder supporting force F_S as the dependent variable, the curve of the supporting force of supporting cylinder with the radial displacement of the leaf spring was obtained by fitting Eq. (8), as shown in Fig. 9.
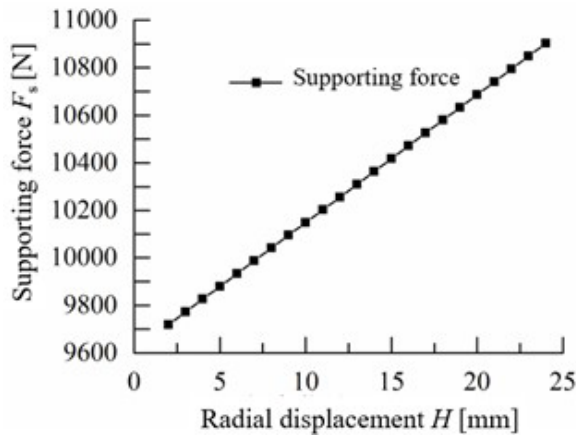

Fig. 9. *Curve of supporting force with radial displacement*

Table 2. *Supporting force of different wellbore*

Wellbore size [mm]	H [mm]	F_2 [N]	F_S [N]
178 (7-inch)	24	1,784	10,901
165 (6.5-inch)	15	1,120	10,417
152 (6-inch)	11	825	10,203

From Fig. 9, the magnitude of the required supporting force was obtained for different wellbore pipes with a design traction force of 10,000 N. From Eq. (7), it can be obtained that the radial displacement of the leaf spring needs to be greater than 8.6 mm to overcome the frictional resistance of the O-ring of 647 N and to have the ability to automatically unlock. Therefore, only the movement of the spring-type of traction robot in 152 mm (140 mm ID), 165 mm (148 mm ID) and 178 mm (161 mm ID) wellbore pipe was studied. From Eq. (7) and Fig. 9, the elastic restoring

force and the required supporting force of the spring-type of anchoring arm can be obtained when different wellbores move, as shown in Table 2.

3 MODELING AND SIMULATION ANALYSIS

In this chapter, using ABAQUS and ADAMS [24] for co-simulation, a rigid-elastic coupled dynamic model was established and compared with the rigid model to verify the superiority of the rigid-elastic coupled dynamic model. Whether the spring-type of anchoring mechanism satisfied the anchoring performance under its design traction force was further verified. Finally, the maximum traction force of the spring-type of anchoring mechanism under different wellbores was determined.

3.1 Rigid-elastic Coupling Model of a Spring-type of Anchoring Mechanism

ABAQUS was carried out to establish a elastic model of the spring-type of anchoring arm. The procedure was as follows:

The spring-type of anchoring arm of the final structure determined in Chapter 2 is used to establish a three-dimensional model. The three-dimensional model was imported into the ABAQUS software. The material properties were defined in the software (the elastic modulus was 2.06×10^5 MPa, the Poisson's ratio was 0.29, and the mass density was 7.85×10^6 kg/mm³). Two connection points of the spring leaf were defined as hard points, constraints were added, modal analysis was carried out to determine the form of the model, and a modal neutral file can be obtained. Finally, the modal neutral file was exported as an mnf file.

After the simulation model of spring-type of anchoring mechanism was built in the SolidWorks software, it would be imported into the ADAMS software. The three components of the left joint of the leaf spring, the right joint of the leaf spring and the fixed connecting rod, which were in a fixed relationship, were integrated into one component through a Boolean operation. Then they were called a "fixed connection body". At this point, the leaf spring is still a non-deformable rigid spring, and the model is rigid. Then, the modal neutral file of mnf of the spring was imported into ADAMS to replace the rigid spring. A rigid-elastic coupled dynamics model was generated, as shown in Fig. 10. The rigid model can be compared with the rigid-elastic coupled model for simulation.
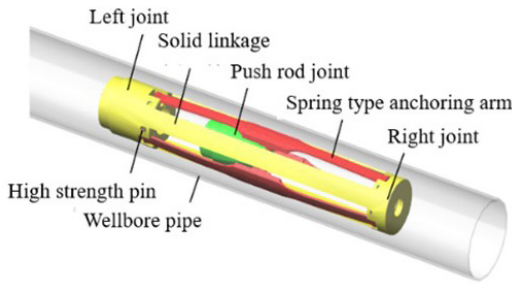
Fig. 10. *Rigid-elastic coupled dynamics model*

To perform dynamic analysis on the rigid-elastic coupled model, it is necessary to define the way of movement between the two contact mechanisms of the model, so that the model has a unique kinematic regularity. The wellbore is defined as a fixed frame, namely a fixed pair. The motion mode between the spring and the left and right support frames is defined as the rotational pair, with a total of six rotational pairs. The motion mode between the spring and the push rod joint is defined as the moving pair, and the motion mode between the central axis and the left and right support frames is defined as the moving pair, with a total of five moving pair.

From the dynamic analysis, it can be known that traction robot was mainly affected by the supporting force F_S and its reaction force F_S', the traction force F_T, the restoring force F_2 of the leaf spring and the friction force f in the traction process. From Table 2, when the traction robot drags the load forward in the 178 mm wellbore, the push rod joint was subjected to a supporting force of 10,901 N, and the fixed body was subjected to a reaction force of the supporting force of 10,901 N and a reaction force of the traction force of 10,000 N. The above loads were applied to the rigid-elastic coupled dynamic model.

In addition, the quality of the spring-type of anchoring mechanism is about 8 kg. Its gravity is 80 N, which can be neglected compared with other forces of several thousand N. The contact between the push rod joint and three spring-types of arms of anchoring mechanisms, and the contact between three leaf-spring and the wellbore were defined as "collision constraint", and the contact type was "spring-type of body to rigid body". The parameter values that used ADAMS to simulate and analyse contact pairs are shown in Table 3. "Contact resilience factor" is the stiffness, which reflects the ability of the two contacting bodies to resist deformation. "Force index" is used to calculate the index of the contribution of the material stiffness term in the instantaneous normal force.

Table 3. *Calculating parameters of contact force*

Parameters	Numerical value
Coefficient of static friction between the spring-type of anchoring arm and pipe wall (μ_1)	0.5
Coefficient of dynamic friction between the spring-type of anchoring arm and pipe wall (μ_2)	0.25
Contact resilience factor [N/mm]	10^5
Force index	1.5
Damping coefficient [N×s/mm]	1,000
Penetration depth [mm]	0.01

3.2 Simulation Analysis of Influencing Factors of Mechanical Characteristics of Spring-type of Anchoring Mechanism

Using the ADAMS/View software, the rigid model and the rigid-elastic coupling model were used to simulate the friction curve and the velocity curve of radial displacement of the spring-type of anchoring arm. In the initial state, a support force of 10,901 N and a load traction force of 10,000 N are applied to the two models respectively for five seconds, and the results are shown in Figs. 11 and 12.
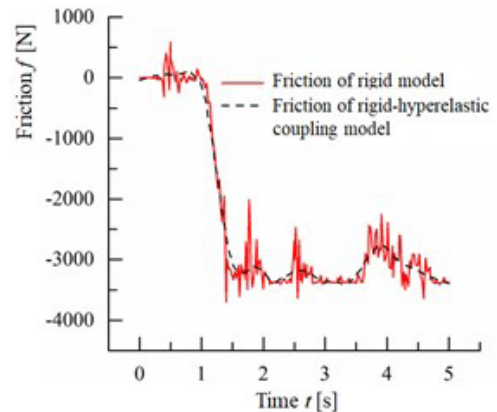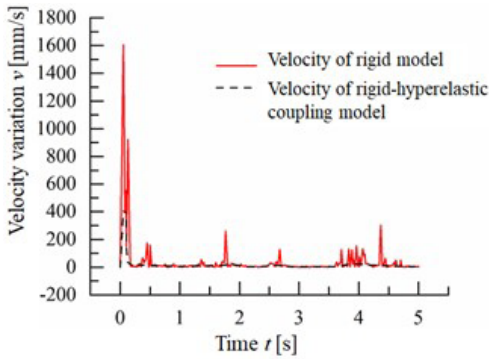

Fig. 11. *Friction curve of rigid model and rigid-elastic coupling dynamic model*

It can be seen from Figs. 11 and 12 that the rigid-elastic coupling model was more stable, more accurate, and superior to the rigid model data. The rigid-elastic coupling model can better reflect the motion characteristics of the spring-type of anchoring mechanism. Therefore, the rigid-elastic coupling model was used to simulate the spring-type of anchoring mechanism. The initial state of the rigid-elastic coupled model was loaded for 5 seconds, during which the force and velocity changes can be obtained.

Fig. 12. *Velocity curve of rigid model and rigid-elastic coupling dynamic model*

Fig. 13 shows the force and velocity curves of the traction process of the spring-type of anchoring mechanism under the conditions of the supporting force of 10,901 N and the traction force of 10,000 N.

It can be seen from Fig. 13 that the friction force on a spring-type of anchoring arm also remained fluctuating around 3,333 N, which is the theoretical frictional force obtained from Eq. (3), after the traction force reached 10,000 N to maintain the level. This phenomenon indicated that the friction force generated by three spring-type of anchoring mechanism (about 10,000 N) can overcome the traction force to anchor the wellbore wall. The velocity of radial displacement started to fluctuate when it was first stressed, and finally gradually remained stationary with the wellbore wall. It indicated that the theoretically calculated supporting force of 10,901 N was able to overcome the traction force of 10,000 N applied to the traction robot to keep it locked with the wellbore wall.
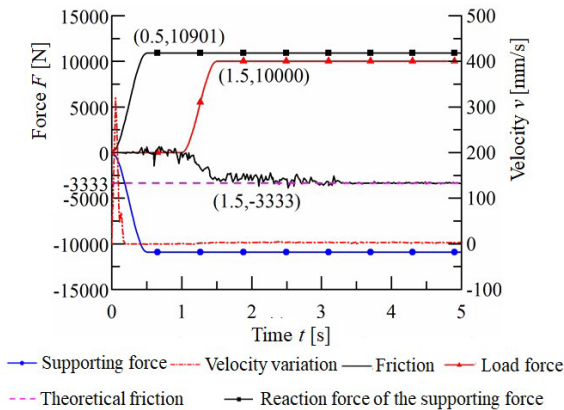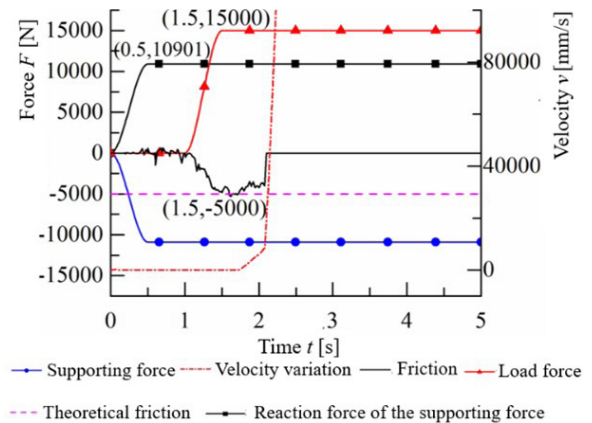

Fig. 13. *Force and velocity curves of the spring-type of anchoring mechanism (10,000 N)*

Figs. 14 and 15 show the force and velocity curves of radial displacement of the spring-type of

anchoring mechanism in the 178 mm wellbore with traction forces of 14,000 N and 15,000 N respectively when the supporting force of 10,901 N remained constant.
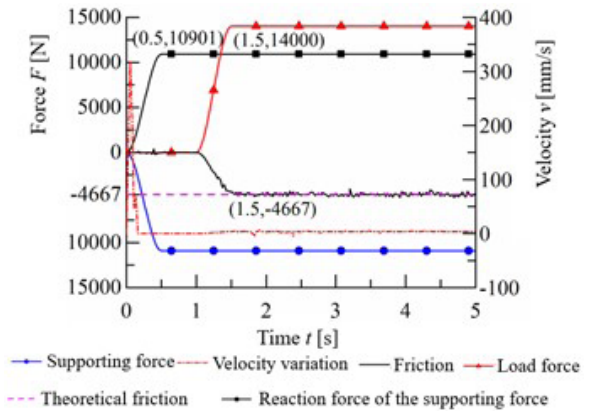
Fig. 14. *Force and velocity curves of the spring-type of anchoring mechanism (14,000 N)*
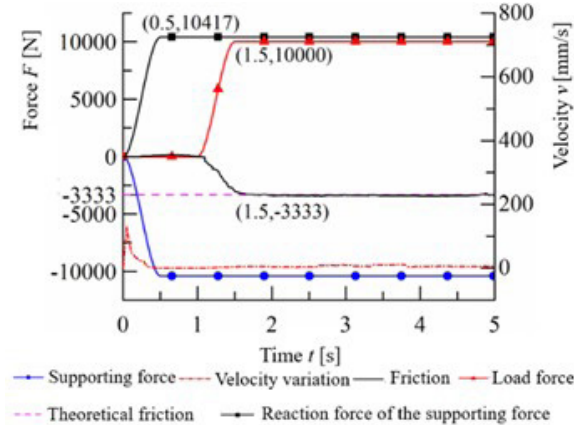

Fig. 15. *Force and velocity curves of the spring-type of anchoring mechanism (15,000 N)*

From Figs. 14 and 15 it can be observed that the spring-type of anchoring mechanism could continue anchoring when the traction force was 14,000 N. When the traction force was 15,000 N, it broke away from the wellbore wall after 1.9 s, and the anchoring failed. This phenomenon demonstrated that the anchoring mechanism cannot conquer the traction force of 15,000 N under the supporting force of 10,901 N, and the traction robot cannot sustain the anchoring with the wellbore wall. Thus, the maximum traction force interval of the spring-type of anchoring mechanism was gained between 14,000 N and 15,000 N in a 178 mm wellbore.

In order to observe the anchoring ability of the spring-type of traction robot under other sizes of the

wellbores, the motion of the traction robot in 165 mm wellbore and 152 mm wellbore was selected as the object of study in this paper. Their anchoring performance was simulated and analysed by applying theoretical supporting force of 10,417 N and 10,203 N respectively, as shown in Figs. 16 to 19.

Fig. 16. *Force and velocity curves of anchoring mechanism in 165 mm wellbore (10,000 N)*

Similarly, it can be understood from Figs. 16 to 19 that the spring-type of anchoring mechanism was able to conquer the traction force of 10,000 N under the supporting force of 10,417 N in a 165 mm wellbore and 10,203 N in a 152 mm wellbore, respectively, to anchor it with the wellbore wall. The maximum traction force interval of the spring-type of traction robot was 12,000 N to 13,000 N and 10,000 N to 11,000 N separately.
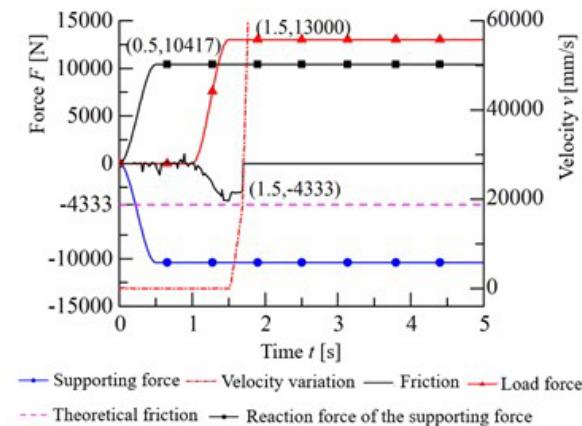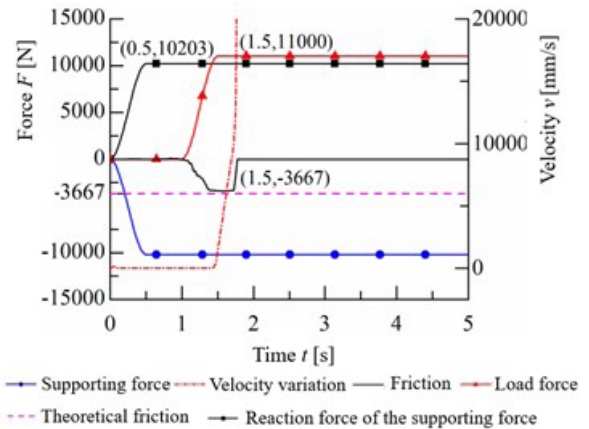

Fig. 17. *Force and velocity curves of anchoring mechanism in 165 mm wellbore (13,000 N)*

It was verified that the spring-type of traction robot can preserve anchoring under a design traction force of 10,000 N with 152 mm, 165 mm and 178 mm

wellbores. At the same time, the maximum theoretical traction force intervals of 10,000 N to 11,000 N, 12,000 N to 13,000 N, and 14,000 N to 15,000 N were acquired for the corresponding sizes of wellbores. It was indicated that the maximum traction force of the traction robot would increase with the increase of the wellbore pipe diameter.
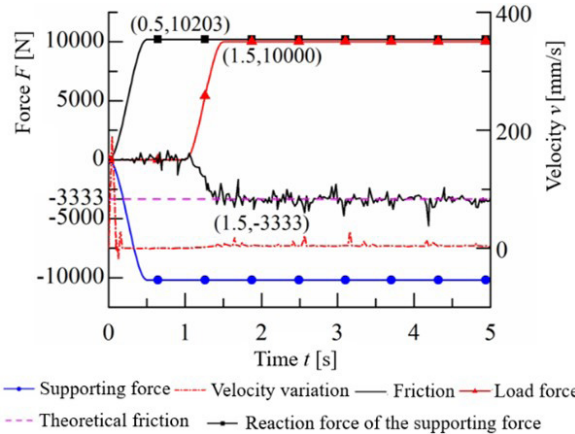
Fig. 18. *Force and velocity curves of anchoring mechanism in 152 mm wellbore (10,000 N)*

Fig. 19. *Force and velocity curves of anchoring mechanism in 152 mm wellbore (11,000 N)*

4 EXPERIMENTAL RESEARCH

The spring-type of anchoring arm of the final structure (span of 462 mm, chamfer radius of 40 mm, width of 30 mm and thickness of 5 mm) determined in Chapter 2 was made into an experimental prototype, which is shown in Fig. 20.

Fig. 20. *Spring-type of anchoring mechanism*

A simulation diagram of the experimental prototype is shown in Fig. 21 to better present its structure. The prototype was used to verify that the spring-type of anchoring mechanism can overcome the traction force of load to achieve anchoring to the wellbore wall under the theoretical support force of the supporting cylinder. The actual maximum traction force of the traction robot can be obtained from the prototype experiment. Also, the recovery effect of the spring-type of anchoring arm was observed after the unloading of the anchoring mechanism.

4.1 Experimental Steps

The experimental scheme of the anchoring mechanism of the spring-type of traction robot is shown in Fig. 22. The experimental procedure of the traction process was as follows:

(1) Hydraulic cylinder 1 was injected with liquid, so that the spring-type of anchoring arms contacted the wellbore wall. Then the voltage signal of the S-shaped pressure sensor was recorded.

(2) Hydraulic cylinder 1 continued to have fluid injected, so that the cylinder generated a supporting force of 10,901 N (voltage signal of S-shaped sensor is 4.48 V).

(3) Hydraulic cylinder 2 was filled with fluid, so that the hydraulic pressure in the cylinder reached 10,000 N (voltage signal of the spoke sensor is
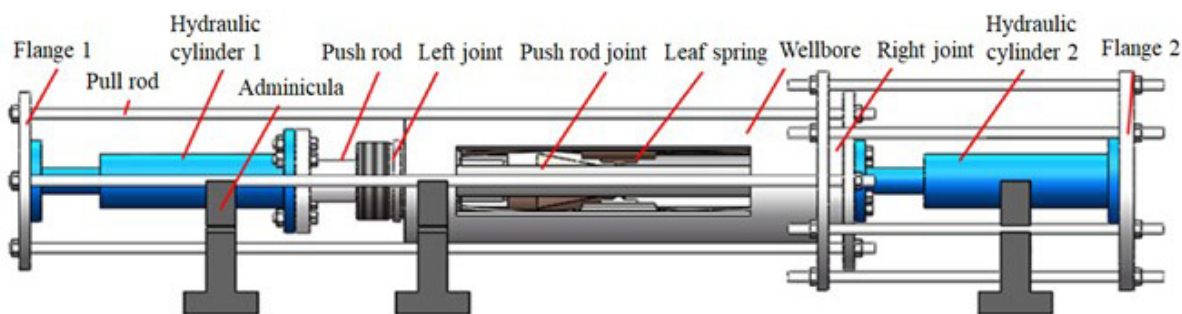

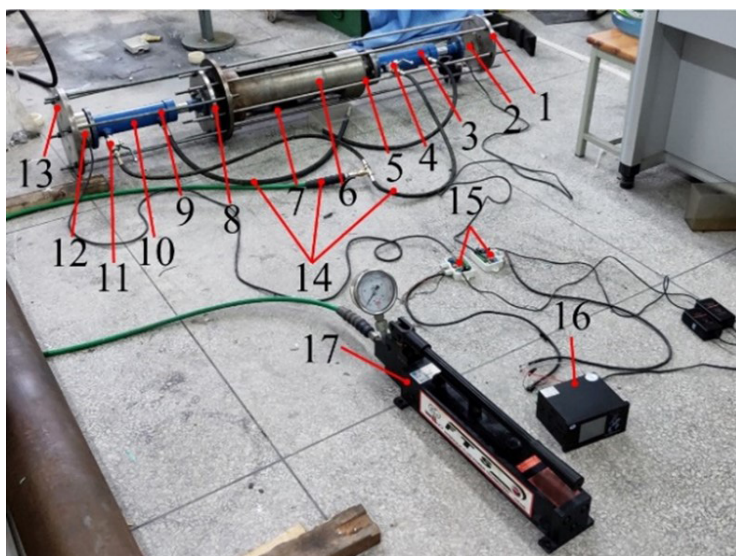**Fig. 21.** *Schematic diagram of experimental equipment*

Fig. 22. *Experimental scheme and experimental system of spring-type of anchoring mechanism; 1 and 8 -flange 1, 2 s-type pull pressure sensor, 3 hydraulic cylinder 1, 4 and 11 manual high-pressure ball valve, 5 and 9 pull rod, 6 178 mm of wellbore pipe, 7 spring-type of anchoring mechanism, 10 hydraulic cylinder 2, 12 spoke pull pressure sensor, 13 flange 2, 14 hydraulic tube, 15 pressure transmitter, 16-Paperless recorder, 17-Manual high-pressure pump*

0.76 V). The anchoring condition of the anchoring mechanism was recorded.

(4) If the anchoring mechanism anchored the wellbore wall, hydraulic cylinder 1 continued to add pressure until the wellbore moved to the right. Also, the pressure in hydraulic cylinder 2 was recorded when the wellbore moved.

(5) Then, finally, the pressure in hydraulic cylinder 2 and hydraulic cylinder 1 was removed to observe the recovery of the spring-type of anchoring arm.

All measuring instruments had been calibrated before the experiment. All experimental instruments have a temperature compensation function, and the temperature has no effect on the measurement data. Therefore, the experimental errors are within the allowable range.

4.2 Experimental Results

The voltage data collected by the paperless recorder were converted into pressure data using the proportional coefficient. The pressure variation curves in hydraulic cylinder 1 (supporting force) and hydraulic cylinder 2 (traction force) are obtained as shown in Fig. 23.
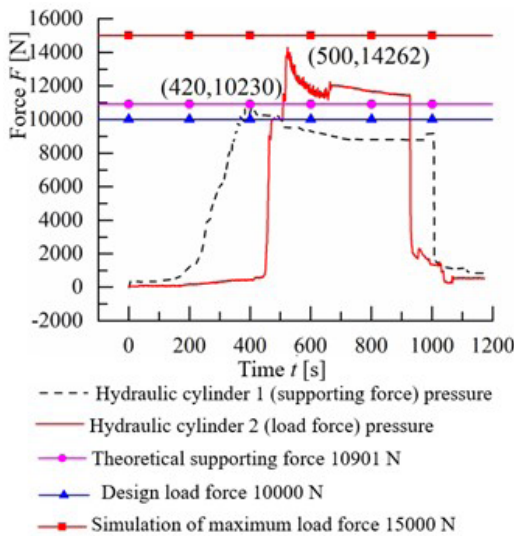

Fig. 23. *Theoretical and experimental support force curve*

Fig. 23 shows that after 400 s the pressure in hydraulic cylinder 1 (supporting force) was kept at 10,230 N, and the pressure in hydraulic cylinder 2 was maintained at about 10,000 N. The spring-type of anchoring mechanism remained relatively stationary with the wellbore. The reasonableness of the theoretical calculation was verified. The anchoring state between the anchoring mechanism and the

wellbore wall is shown in Fig. 24, and the distance between the wellbore and the flange was 30 mm.
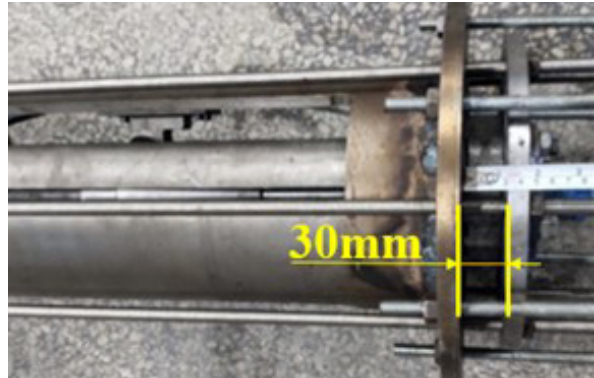

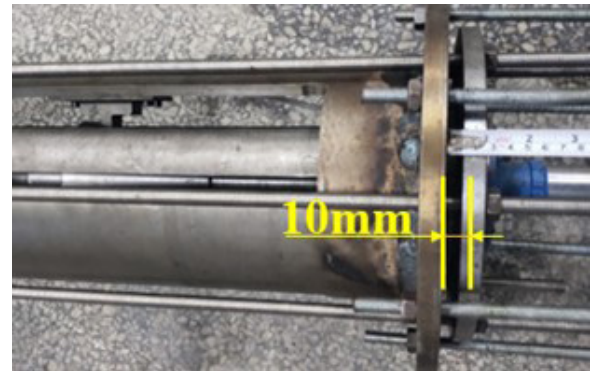**Fig. 24.** *Anchoring state of spring-type of anchoring mechanism*

Fig. 25. *Anchoring failure state of spring-type of anchoring mechanism*

Continuing to feed liquid to hydraulic cylinder 2, its pressure was increased to 14,262 N and then began to decrease, while the pressure of hydraulic cylinder 1 began to decrease. Here relative sliding occurred between the anchoring mechanism and the wellbore wall, and the anchoring failed. It was illustrated that the maximum traction force was 14,262 N. The relative position of the wellbore and the spring-type of anchoring mechanism is shown in Fig. 25 after the experiment, and the distance between the wellbore and the flange was 10 mm.

Table 4. *Comparison of theoretical and experimental data of support force and traction force*

	The supporting force	The maximum traction force
Experimental value [N]	10,230	14,262
Simulation value [N]	10,901	15,000
Deviation [%]	6.1	4.9

From Table 4, the experimental results showed that the simulation values did not differ much from the experimental values. the correctness of the mechanical analysis, the optimization of the leaf spring and the rigid-elastic coupling model were verified. However, the experimental results also exposed some problems. After hydraulic cylinder 1 was decompressed, the spring did not reset quickly, and only slowly retreated after an external force was applied. The reason for this was due to safety concerns. Hydraulic cylinder 1 released the pressure slowly, so that the elastic restoring force of the spring-type of anchoring arm was also slowly reduced, and resulted in the arm returning slowly.

5 CONCLUSIONS

(1) In this paper, a novel spring-type of anchoring mechanism of a traction robot based on inclined blocks was proposed, which can provide a large traction force for the robot and can avoid being stuck. Meanwhile, the mechanical analysis of the traction process was completed, and the structure of the spring-type of anchoring mechanism was optimized.

(2) Through establishing the rigid-elastic coupling model of the spring-type of anchoring mechanism, it was determined that the rigid-elastic coupling model can better reflect the motion characteristics of the traction robot compared with the rigid model. At the same time, through analysis of the rigid-elastic coupling model simulation, the correctness of the theoretical mechanical calculation of the spring-type of anchoring mechanism was verified, and the maximum traction force under different structural parameters was obtained.

(3) Through the experiment, it was verified that the experimental supporting force required to overcome the load of 10,000 N was 10,230 N, which was 6.1 % different from the theoretically calculated value. The maximum traction force that the traction robot anchoring mechanism can provide was 14,262 N, which was 4.9 % different from the simulated calculated value. The experiment result showed the correctness of the theoretical calculation, the optimization of the structure of the anchoring arm, and the simulation of the rigid-elastic coupling model.

The research results of this paper lay a foundation for the structural design and engineering application of spring-type of traction robot. It can effectively ensure the downhole safety of oil and gas wells.

6 ACKNOWLEDGEMENTS

7 REFERENCES

[1] Saeed A., French, A., Moore, N.B. (2020). Analysis and case study: Comparing CT slim tractor performance using different CT sizes in 3 wells. *SPE/ICoTA Well Intervention Conference and Exhibition*, art. ID SPE-199871-ms, **DOI:10.2118/199871-ms**.

[2] Zhao, J., Han, S., Liu, Q., Zhang, Y., Xiao, X., Dong, R., Fang, S., Tu, C. (2022). Combined control mechanism of weight on bit and rate of penetration with a downhole robot in the coiled-tubing drilling process. *SPE Journal*, vol. 27, no. 1, p. 153-166, **DOI:10.2118/208570-PA**.

[3] Alsaiood, H., Otaibi, A., Duthie, L., Aybar, U., French, A. (2020). Powerful hydraulic coil tubing tractor facilitates stimulation application in extended reach wells thru completion operations. *SPE/ICoTA Well Intervention Conference and Exhibition*, art. ID SPE-199851-MS, **DOI:10.2118/199851-ms**.

[4] He, L., McAllister, J., Hawkins, J., Turner, M. (2020). Application of downhole tractor in gas well zonal isolation. *SPE/ICoTA Well Intervention Conference and Exhibition*, art. ID SPE-199830-MS, **DOI:10.2118/199830-ms**.

[5] Xiao, X., Dai, J., Zhu, H., Zhao, J. (2021). Experimental and numerical simulation research on eccentric flow channel erosion of drilling robot. *Journal of Southwest Petroleum University (Science & Technology Edition)*, vol. 43, no. 2, p. 167-177, **DOI:10.11885/j.issn.1674 5086.2020.11.02.01**. (in Chinese)

[6] Badeghaish, W., Noui-Mehidi, M.N., Al-Mulhem, A.A. (2018). Comprehensive review of well tractor technology in highly extended reach wells. *SPE/ICoTA Coiled Tubing and Well Intervention Conference and Exhibition*, art. ID SPE-189906-MS, **DOI:10.2118/189906-ms**.

[7] Denney, D. (1999). Wireline-tractor production logging in horizontal wells. *Journal of Petroleum Technology*, vol. 51, no. 3, p. 80-81, **DOI:10.2118/0399-0080-JPT**.

[8] Heaney, F.M., Lee, M.L., Gupta, S. (2022). New torque balancing algorithm improves pulling force and speed with wireline electro-mechanical tractor. *SPE/ICoTA Well Intervention Conference and Exhibition*, art. ID SPE-209010-MS, **DOI:10.2118/209010-ms**.

[9] Saeed, A., Duthie, L., Yaklovlev, T., Sagr, H. (2017). Development and world's first field deployment of 2.125? tridem coiled tubing tractor for extended reach open hole horizontal wells with ESP completions. *Abu Dhabi International Petroleum Exhibition & Conference*, art. ID SPE-188283-MS, **DOI:10.2118/188283-ms**.

[10] Tyagi, C., Singh, V., Nayak, J.P., Pinto, T. (2017). Unique milling bit deployed via e-line intervention enables operator to achieve early production. *SPE/ICoTA Coiled Tubing and Well Intervention Conference and Exhibition*, art. ID SPE-184786-MS, **DOI:10.2118/184786-ms**.

[11] Formica, J., Wise, J., Boye-Moller, C., Davis, B., Godfrey, B., Walker, C. (2004). Tractor-conveyed sensors and chemical packer are utilized to remediate an extended-reach horizontal uncemented slotted liner completion in a siliceous shale reservoir, Kern County, California, USA. *SPE International Thermal Operations and Heavy Oil Symposium and Western Regional Meeting*, art. ID SPE-86938-MS, **DOI:10.2118/86938-ms**.

[12] Nakazato, Y., Sonobe, Y., Toyama, S. (2012). Development of in-pipe micro mobile robot using peristalsis motion driven by hydraulic pressure. *Micromechanics and Microactuators, Mechanisms and Machine Science*, vol. 2, p. 23-29, **DOI:10.1007/978-94-007-2721-2_3**.

[13] Grigore, L.S., Oncioiu, I., Priescu, I., Joita, D. (2021). Development and evaluation of the traction characteristics of a crawler EOD robot. *Applied Sciences*, vol. 11, no. 9: art. ID 3757, **DOI:10.3390/app11093757**.

[14] Nagase, J.Y., Fukunaga, F., Shigemoto, Y. (2017). Cylindrical elastic crawler mechanism for pipe inspection. *Advances in Cooperative Robotics*, p. 304-311, **DOI:10.1142/9789813149137_0037**.

[15] Gao, S., Li, C., Sun, W. (2014). Structural design and mechanical analysis of expansion brake for downhole tractor. *Science & Technology Information*, vol. 12, no. 19, p. 92-95, **DOI:10.16661/j.cnki.1672-3791.2014.19.170**.

[16] Liu, Q., Zhao, J., Zhu, H., Zhang, W. (2019). Mechanical model of drilling robot driven by the differential pressure of drilling fluid. *Arabian Journal for Science and Engineering*, vol. 44, p. 1447-1458, **DOI:10.1007/s13369-018-3578-3**.

[17] Liu Q., Zheng W., Yang Y., Zhang S., Zhu H. (2018). Two-way locking mechanism design for telescopic downhole tractors. *Journal of Southwest Petroleum University (Science & Technology Edition)*, vol. 40, no. 1, p. 1, DOI:10.11885/j.issn.1674-5086.2016.12.24.01. (in Chinese)

[18] He, C., Zhao, J., Li, Z., Wang, Z., Han, S., Zhang, Y., Xiao, J. (2021). Design method and mechanical analysis of gripping mechanism of drilling robot. *Arabian Journal for Science and Engineering*, p. 11197-11209, **DOI:10.1007/s13369-021-05898-9**.

[19] Yaakoubi, M., Kchaou, M., Dammak, F. (2013). Simulation of the thermomechanical and metallurgical behavior of steels by using ABAQUS software. *Computational Materials Science*, vol. 68, p. 297-306, **DOI:10.1016/j.commatsci.2012.10.001**.

[20] Zhao, J., Peng, H., Fang, S., Wang, K., Han, S., Zhang, Y., Zhu, Z., Tu, C. (2021). Study on dynamic sealing performance of combined sealing structure of telescopic type of downhole robot by using HTHP coupling method. *Science Progress*, vol. 104, no. 3, **DOI:10.1177/00368504211013214**.

[21] Xu, F. (1989). *Calculation of Friction Force Caused by O-ring*. *Petroleum Machinery*, no. 08, pp. 9-10+35. (in Chinese)

[22] Xiao, S. (2001). Calculation of frictional force of o-type sealing ring in hydraulic vat. *Journal of Southern Institute of Metallurgy*, no. 1, p. 18-20, **DOI:10.13265/j.cnki.jxlgdxxb.2001.01.005**. (in Chinese)

[23] Zuo, X., Zhang, J. (1989). Study on Friction Force of O-type Auxiliary Seal Ring of Mechanical Seals. *Journal of Fluid Engineering*, no. 04, p. 1-8. (in Chinese)

[24] Yan, H., Li, J., Kou, Z., Liu, Y., Li, P., Wang, L. (2022). Research on the traction and obstacle-surmounting performance of an adaptive pipeline-plugging robot. *Strojniški vestnik - Journal of Mechanical Engineering*, vol. 68, no. 1, p. 14-26, **DOI:10.5545/sv-jme.2021.7361**.